



1     **Retrieval of dominant methane (CH<sub>4</sub>) emission sources, the first high resolution**  
2                     **(1-2m) dataset of storage tanks of China in 2000-2021**

3     Fang Chen<sup>1, 2, 3, †</sup>, Lei Wang<sup>1, 2, 4, †</sup>, Yu Wang<sup>5, 6, \*</sup>, Haiying Zhang<sup>1, 2</sup>, Ning Wang<sup>7</sup>,  
4     Pengfei Ma<sup>5, 6</sup>, Bo Yu<sup>1, 2, 4, \*</sup>

5     <sup>1</sup>International Research Center of Big Data for Sustainable Development Goals, Beijing,  
6     100094, China

7     <sup>2</sup>Key Laboratory of Digital Earth Science, Aerospace Information Research Institute,  
8     Chinese Academy of Sciences, Beijing, 100094, China

9     <sup>3</sup>University of Chinese Academy of Sciences, Beijing, 100049, China

10    <sup>4</sup>School of Computer Science and Information Security, Guilin University of Electronic  
11    Technology, Guilin, 541004, China

12    <sup>5</sup>State Environmental Protection Key Laboratory of Satellite Remote Sensing, Beijing  
13    100094, China;

14    <sup>6</sup>Satellite Application Center for Ecology and Environment, Ministry of Ecology and  
15    Environment, Beijing 100094, China;

16    <sup>7</sup>College of Urban and Environmental Sciences, Peking University, Beijing, 100871,  
17    China

18    † These authors contributed equally to this work and should be considered as co-first  
19    authors

20    \*Corresponding author: Yu Wang (chenfang\_group@163.com), Bo Yu  
21    (yubo@radi.ac.cn)

22

23    **Abstract.** Methane (CH<sub>4</sub>) is a significant greenhouse gas in exacerbating climate  
24    change. Approximately 25% of CH<sub>4</sub> is emitted from storage tanks. It is crucial to  
25    spatially explore the CH<sub>4</sub> emission patterns from storage tanks for efficient strategy  
26    proposals to mitigate climate change. However, due to the lack of publicly accessible  
27    storage tank locations and distributions, it is difficult to ascertain the CH<sub>4</sub> emission  
28    spatial pattern over a large-scale area. To address this problem, we generated a storage  
29    tank dataset (STD) by implementing a deep learning model with manual refinement  
30    based on high spatial resolution images (1-2m) from the GaoFen-1, GaoFen-2, GaoFen-  
31    6, and Ziyuan-3 satellites over cities in China with officially reported numerous storage  
32    tanks in 2021. STD is the first storage tank dataset over 92 typical cities in China. The  
33    dataset can be accessed at <https://zenodo.org/records/10514151> (Chen et al., 2024). It  
34    provides a detailed georeferenced inventory of 14,461 storage tanks, wherein each  
35    storage tank is validated and assigned the construction year (2000-2021) by visual  
36    interpretation referring to the collected high spatial resolution images, historical high  
37    spatial resolution images of Google Earth, and field survey. The inventory comprises  
38    storage tanks having various distribution patterns in different cities. Spatial consistency  
39    analysis with CH<sub>4</sub> emission product shows good agreement with storage tank  
40    distributions. The intensive construction of storage tanks significantly induces CH<sub>4</sub>  
41    emissions from 2005 to 2020, underscoring the need for more robust measures to curb



42 CH<sub>4</sub> release and aid in climate change mitigation efforts. Our proposed dataset STD  
43 will foster the accurate estimation of CH<sub>4</sub> released from storage tanks for CH<sub>4</sub> control  
44 and reduction and ensure more efficient treatment strategies are proposed to better  
45 understand the impact of storage tanks on the environment, ecology, and human  
46 settlements.

47

## 48 **1. Introduction**

49 The Industrial Revolution witnessed a continuous increase in greenhouse gases,  
50 resulting in global climate warming (Zhang et al., 2021). Methane (CH<sub>4</sub>) is the second  
51 dominant anthropogenic greenhouse gas to global climate warming with a contribution  
52 of 20% (Kirschke et al., 2013) after carbon dioxide (CO<sub>2</sub>). Meanwhile, CH<sub>4</sub> is more  
53 effective in trapping heat, with 85 times more climate warming potency than CO<sub>2</sub>  
54 (Stocker, 2014). The atmospheric lifetime of CH<sub>4</sub> is approximately 10 years, which is  
55 shorter than most other greenhouse gases; thus, reducing CH<sub>4</sub> emissions is more cost-  
56 effective in lowering the climate warming potential impact (Lin et al., 2021; Montzka  
57 et al., 2011). CH<sub>4</sub> is emitted mainly from energy-related activities and petrochemical  
58 processes (Ding et al., 2017; Fan et al., 2023). Storage tanks, defined as large  
59 containers of crude oil or other petroleum, and industrial materials, such as alcohols,  
60 gases, or liquids, are among the most significant sources of emitting CH<sub>4</sub> (Im et al.,  
61 2022; Johnson et al., 2022). Without an adequate control or management strategy, large  
62 amounts of CH<sub>4</sub> will escape into the atmosphere (Im et al., 2022). From a greenhouse  
63 gas control standpoint, it is of great interest to examine the distribution patterns of the  
64 storage tanks. With a detailed and comprehensive storage tank inventory, we can  
65 effectively estimate the spatial pattern of CH<sub>4</sub> emissions and reduce the risk of CH<sub>4</sub>  
66 emission by installing recovery units (Johnson et al., 2022) to promote sustainable  
67 development goals. However, it is challenging to access detailed distribution records  
68 for storage tanks from the public records in China.

69 Given the advances in remotely sensed technology (Chen et al., 2023; Yu et al.,  
70 2023a; Yu et al., 2023b), the ready availability of high spatial resolution remote sensing  
71 images via the GaoFen series satellites and the Ziyuan-3 satellite provides means to  
72 extract remote sensing data for large-scale storage tanks. Numerous studies on the use  
73 of automatic methods to extract storage tanks from high spatial resolution remote  
74 sensing images have been performed (Fan et al., 2023; Wu et al., 2022; Yu et al., 2021),  
75 including the Hough transform (Yuen et al., 1990), image saliency enhancement (Zhang  
76 and Liu, 2019), support vector machines (Xia et al., 2018), and Res2-Unet+ deep  
77 convolution networks (Yu et al., 2021). The focus of the works above is primarily  
78 spatially limited, and the images collected for extraction are mostly pre-subtracted from  
79 regions known to contain storage tanks. The transferability and the practical  
80 applicability of the proposed methods remain to be clarified. To our knowledge, there  
81 are limited publicly available datasets on storage tanks. Northeast Petroleum  
82 University–Oil Well Object Detection Version 1.0 (NEPU–OWOD V1.0) covers 1,192  
83 oil storage tanks within Daqing City (Wang et al., 2021). This dataset covers the  
84 boundary boxes for each storage tank but lacks details on the storage tank inventory.  
85 Another two datasets, the Oil and Gas Tank Dataset (Rabbi et al., 2020) and the Oil



86 Storage Tank Dataset (Heyer, 2019) acquired via the Kaggle platform, have been  
87 released without georeferenced information and lack detail regarding the contour  
88 shapes. The datasets are generally proposed to improve the performance of algorithms  
89 in storage tank extraction. Currently, most studies are concentrated on algorithm  
90 development for storage tank extraction rather than exploring the spatial distribution of  
91 storage tanks in large-scale areas and the impact of storage tank construction on CH<sub>4</sub>  
92 emission in different areas over the years. The spatial distributions of storage tanks in  
93 China have not yet been investigated and recorded. The lack of storage tank datasets  
94 makes it impossible to estimate the impact of anthropogenic energy-related activities  
95 on CH<sub>4</sub> emission and air pollution.

96 To foster the control and reduction of CH<sub>4</sub> emissions to mitigate climate change  
97 and provide researchers with free access to detailed and georeferenced storage tank  
98 inventory to monitor the corresponding potential impact on the atmosphere and  
99 residential environment over typical cities in China, we compiled a storage tank  
100 inventory based on high spatial resolution images of the GaoFen-1, GaoFen-2, GaoFen-  
101 6, and Ziyuan-3 satellites for cities with intensive storage tanks over China. The cities  
102 are listed by the Ministry of Ecology and Environment of China with intensive storage  
103 tanks and prominent fugitive emissions, inadequate monitoring and control of treatment  
104 measures (Wang et al., 2022). There are 92 cities in total, mainly located in mid-eastern  
105 China. Given that large storage tanks may emit significant levels of CH<sub>4</sub>, storage tanks  
106 of size  $\geq 500$  m<sup>2</sup> were selected as the main target to control the reduction of CH<sub>4</sub> in the  
107 proposed inventory. To this end, we generated a complete inventory of storage tanks of  
108 size  $\geq 500$  m<sup>2</sup> for the 92 cities in China with intensive storage tanks, which were subject  
109 to the implementation of CH<sub>4</sub> reduction measures.

110 In this study, firstly, we collected high spatial resolution images to cover the entire  
111 study area. We pre-processed them to synchronize the pixel intensities of ground objects  
112 in different images from different imaging sensors and study areas. Secondly, we  
113 proposed a semantic segmentation framework to construct the storage tank extraction  
114 model based on the training samples of Ningbo, Tangshan, and Dongying cities. Thirdly,  
115 the constructed model is applied to extract storage tanks in all the other cities to generate  
116 extraction results. Fourthly, the extracted storage tank result images are converted to  
117 vectors, revised and assigned the corresponding construction year by visual  
118 interpretation with reference to the historical high spatial resolution images of Google  
119 Earth, high spatial resolution images collected, and field survey. Fifthly, we explored  
120 the spatial distribution pattern of storage tanks in typical cities in China. Sixthly, we  
121 further explored the consistency of storage tank spatial patterns and CH<sub>4</sub> emission in  
122 the atmosphere and the impact of storage tank construction on time-series CH<sub>4</sub> emission  
123 change from 2005 to 2020. Finally, the uncertainties, limitations, and implications of  
124 our proposed STD dataset are discussed for studying climate change and air pollution.  
125 This new database represents the first inventory to provide a detailed distribution of the  
126 locations, boundaries of the storage tanks, and the corresponding construction year of  
127 each storage tank. The inventory documents the spatial and temporal distribution of  
128 storage tanks of different sizes, and it is hoped that this work will facilitate the  
129 development of environment-friendly regulatory proposals for more effective CH<sub>4</sub>



130 emission control and energy resource management.

## 131 **2. Related works in mapping storage tanks**

132 Storage tank extraction from high spatial resolution images has been of interest for  
133 many years for its significant role in storage and greenhouse gas emission. Generally,  
134 the methods for extracting storage tanks are grouped into three categories. Circle  
135 detection by Hough transformation (O'duda, 1972) and template matching (Hou et al.,  
136 2019); machine learning model construction by morphological, spectral, and textual  
137 feature engineering (Xia et al., 2018); deep learning model construction by continuous  
138 convolution operations (Fan et al., 2023). Deep learning methods have been extensively  
139 used to map storage tanks due to their strong feature learning capability and higher  
140 model transferability.

141 Semantic segmentation is a widely employed deep learning framework in object  
142 extraction by assigning each pixel a semantic label in the image (Chen et al., 2022; Yu  
143 et al., 2022b). Fully convolution network (FCN) (Long et al., 2015) is a basic  
144 framework of semantic segmentation with three components: backbone feature learning,  
145 convolution feature learning with skip architecture, and up-sampling layer to resample  
146 the learned feature map to the same size of the input image. Based on FCN, numerous  
147 frameworks have been inspired, such as SegNet (Badrinarayanan et al., 2017), PSPNet  
148 (Zhao et al., 2017), Unet (Ronneberger et al., 2015), DeepLabv2 (Chen et al., 2017b),  
149 and DeepLabv3 (Chen et al., 2017a). Unet has a widespread use for its easy  
150 implementation and high efficiency. The proposal of Res2-Unet+ framework for  
151 storage tank extraction (Yu et al., 2021; Zalpour et al., 2020) integrates Res2Net module  
152 (Gao et al., 2019) to Unet. Res2Net module is proposed to learn multi-scale features by  
153 learning at a more granular level. It has shown strong applicability in extracting storage  
154 tanks from images of different imaging sensors (Yu et al., 2022a). However, many  
155 storage tank pixels are still omitted due to their similar spectral characteristics with  
156 neighboring ground objects. To resist the shortage, we have proposed a new semantic  
157 segmentation framework based on Res2-Unet+ and enlarged the variability of storage  
158 tank training samples to build a more robust and accurate extraction model.

159

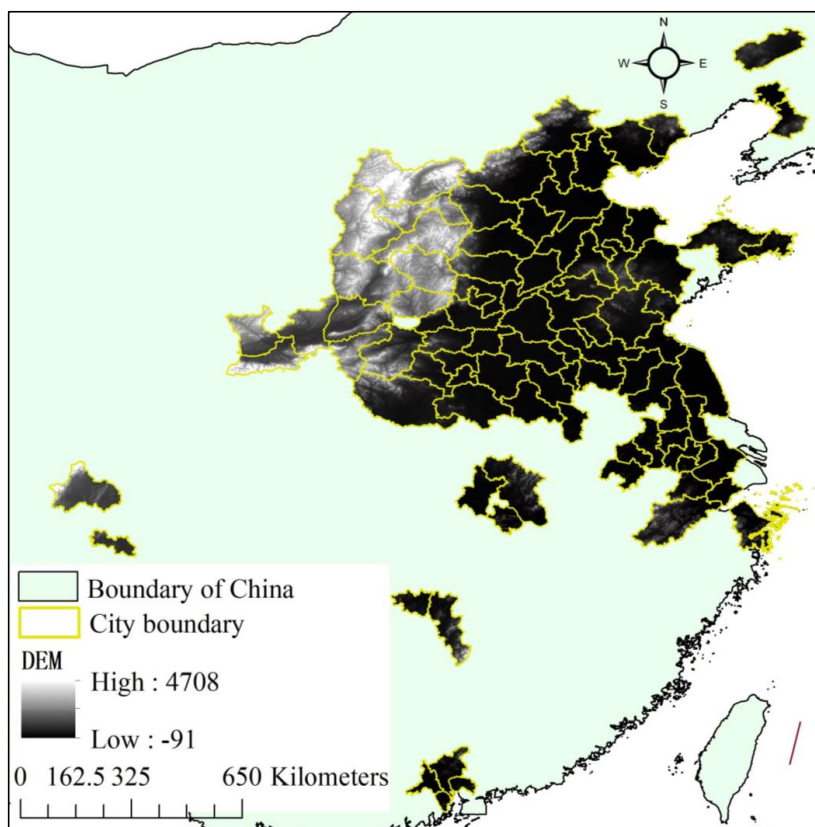
## 160 **3. Data sources**

### 161 **3.1 Study area**

162 The study area covers 92 typical cities (as shown in Figure 1) with intensive  
163 storage tanks over China, assigned by the Ministry of Ecology and Environment of  
164 China (Wang et al., 2022). The typical cities lack detailed monitoring and control of  
165 prominent fugitive emissions, whose effective measurements in CH<sub>4</sub> reduction  
166 emission are urgently demanding and requiring. The 92 cities tended to be located in  
167 mid-eastern China. Many of the cities are located near or next to the boundary of  
168 mainland China. Synthesized with a digital elevation model (DEM) from the product  
169 of the Shuttle Radar Topography Mission (SRTM) (Yang et al., 2011), we can recognize  
170 that most cities are plains. As is acknowledged, plains are densely populated. The large  
171 population numbers will bring more frequent human activities, triggering more  
172 pollutant and greenhouse gas emissions. The lack of efficient measurements in CH<sub>4</sub>



173 reduction will result in a more direct impact on the populations in the residential area.  
174 Therefore, exploring the spatial distribution pattern of storage tanks relative to CH<sub>4</sub>  
175 emission is significant to seek more effective solutions for CH<sub>4</sub> reduction.



176  
177 *Figure 1. Study area demonstration with digital elevation from the Shuttle Radar*  
178 *Topography Mission (SRTM) product.*  
179

### 180 3.2 High spatial resolution images

181 The high spatial resolution images used for extracting storage tanks in the 92 cities  
182 were collected from four satellites: the GaoFen-1, GaoFen-2, GaoFen-6, and Ziyuan-3  
183 satellites in 2021. The images are collected between June and August with the least  
184 cloud coverage (<10%) from the four satellites, when different ground objects have  
185 more pronounced spectral differences, which makes it easier to distinguish storage  
186 tanks from background objects. As listed in Table 1, the images for the GaoFen-1,  
187 GaoFen-6, and Ziyuan-3 satellites have a spatial resolution of 2 m, and those for the  
188 GaoFen-2 have a spatial resolution of 1 m after fusion of the multispectral image and  
189 the panchromatic image. Referring to Table 1, we can recognize that 4,403 images were  
190 collected. The places covered with multiple images are manually screened to one image  
191 with the best imaging quality and least cloud proportion. Based on the screened high  
192 spatial resolution images, multiple image pre-processing steps are performed to



193 synchronize the ground objects in different images of different sensors for different  
 194 study areas, comprising atmospheric correction, radiation correction, geometric  
 195 precision correction, image fusion, image projection, uniform color processing, and  
 196 image mosaicking.

197

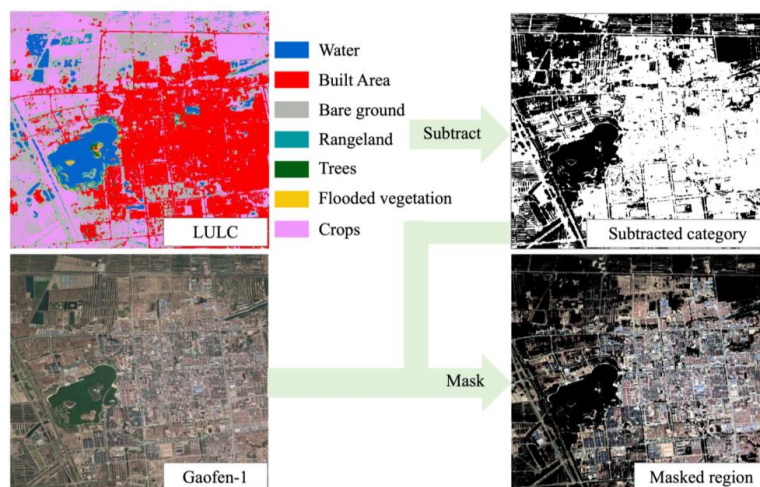
198 *Table 1. Imaging characteristics of each high spatial resolution satellite and the*  
 199 *number of collected images of different satellites covering 92 typical cities in China*  
 200 *between June and August 2021. The notation Pan is short for Panchromatic band,*  
 201 *and Multi represents multi-spectral band*

	<b>GaoFen-1</b>	<b>GaoFen-2</b>	<b>GaoFen-6</b>	<b>Ziyuan-3</b>	<b>Total</b>
<b>Spatial resolution</b>	2m(Pan)/ 8m(Multi)	1m(Pan)/ 4m(Multi)	2m(Pan)/ 8m(Multi)	2m(Pan)/ 6m(Multi)	
<b>Multi-spectral Band</b>	Red/Green/ Blue/Near- Infrared	Red/Green/ Blue/Near- Infrared	Red/Green/ Blue/Near- Infrared	Red/Green/ Blue/Near- Infrared	
<b>Number</b>	1,289	1,330	139	1,645	4,403

202

### 203 **3.3 Land use land cover product**

204 Given that storage tanks are constructed mainly in residential areas, a 10 m land  
 205 use land cover (LULC) product of the Esri Land Cover in 2021 (Karra et al., 2021) is  
 206 used for subtracting the study area to minimize the impact of complex background  
 207 objects in the high spatial resolution images following the workflow as shown in Figure  
 208 2. The land use product of the Esri Land Cover is generated based on the Sentinel-2  
 209 images from the European Space Agency (ESA) with an overall accuracy of 75%  
 210 (Venter et al., 2022), which has been updated every year since 2017. It comprises nine  
 211 ground object categories: water, trees, flooded vegetation, bare ground, crops, snow/ice,  
 212 clouds, rangeland, and built area. Since storage tanks are mostly constructed in urban  
 213 areas, the categories of built area and bare ground are recognized as potential areas for  
 214 constructing storage tanks. Consequently, the corresponding ground object category  
 215 products of built area and bare ground are subtracted from the LULC product 2021 and  
 216 used to mask the high spatial resolution images of the 92 cities, as demonstrated in  
 217 Figure 2. Pixels locating outside the mask in the high spatial resolution images,  
 218 whose intensities are assigned zero. The masked high spatial resolution images of the  
 219 92 cities are further used for storage tank extraction.



220  
221 *Figure 2. Subtraction of potential area with storage tanks from high spatial resolution*  
222 *images.*  
223

### 224 3.4 CH<sub>4</sub> product image

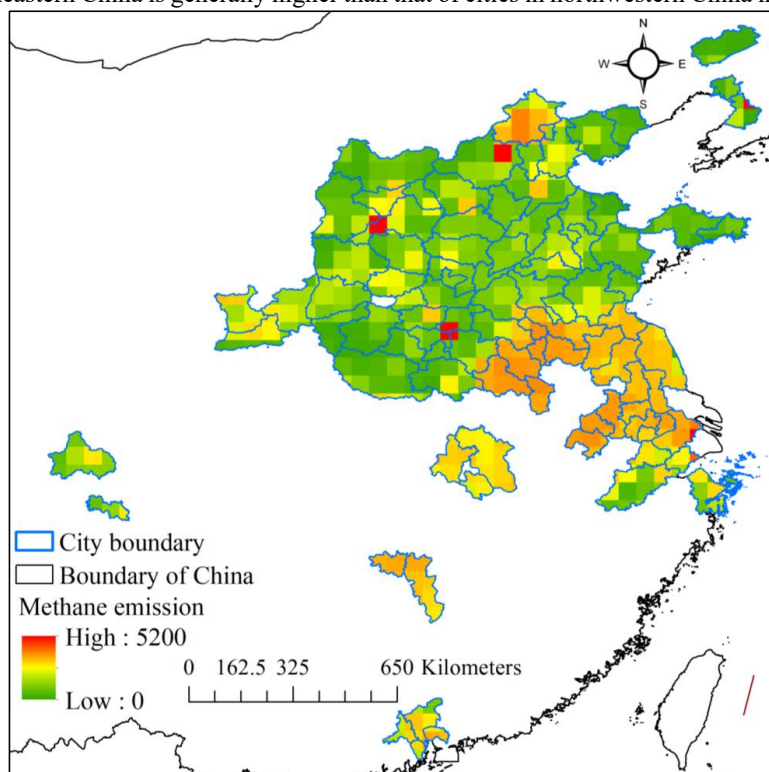
225 As storage tanks are a dominant source of CH<sub>4</sub> emission, we have collected CH<sub>4</sub>  
226 emission products to explore the spatial consistency of CH<sub>4</sub> with the density of storage  
227 tanks and the impact of storage tank construction over time on CH<sub>4</sub> emission. There  
228 have been many CH<sub>4</sub> emission product images proposed, including the Community  
229 Emission Data System (CEDS) (Hoesly et al., 2018), the product from Peking  
230 University (Peng et al., 2016), the Emissions Database for Global Atmospheric  
231 Research (EDGAR) (Crippa et al., 2019), the Regional Emission Inventory in Asia  
232 (REAS) (Kurokawa et al., 2013), and Greenhouse Gas and Air Pollution Interactions  
233 and Synergies (GAINS and ECLIPSE) (Amann et al., 2011). Since our collected high  
234 spatial resolution remote sensing images were taken in the year 2021, the spatial  
235 consistency and the impact of storage tank construction on CH<sub>4</sub> emission are explored  
236 using the CH<sub>4</sub> emission product of GAINS, which offers a comprehensive series of data  
237 accessible to the public (Lin et al., 2021). The dataset of GAINS was selected over the  
238 other four products because the four products lacked continuous updates with limited  
239 temporal coverage until 2015.

240 We adopted the estimated CH<sub>4</sub> emission from energetic activities product of the  
241 ECLIPSE V6b Baseline scenario from GAINS. It is a global annual product with a  
242 spatial resolution of 0.5° and a temporal coverage of 1990-2050 at an interval of 5 years.  
243 For the estimated CH<sub>4</sub> emission from GAINS in the years 1990-2018, the product is  
244 generated from statistics of the International Energy Agency (IEA), and the years 2019-  
245 2050 are from the outlook of the IEA World Energy Outlook (Lane, 2018). To  
246 synchronize with the temporal scope of storage tank construction from 2000 to 2021,  
247 the CH<sub>4</sub> emission products of 2005, 2010, 2015, and 2020 are collected.

248 As demonstrated in Figure 3, the emission of CH<sub>4</sub> in 2020 varies remarkably in  
249 different areas. There are many clusters of CH<sub>4</sub> emission in the study area, with the



250 highest of 5,160.62 Tg  $\text{CH}_4 \text{ yr}^{-1}$ .  $\text{CH}_4$  in the atmosphere of cities located in  
251 southeastern China is generally higher than that of cities in northwestern China in 2020.

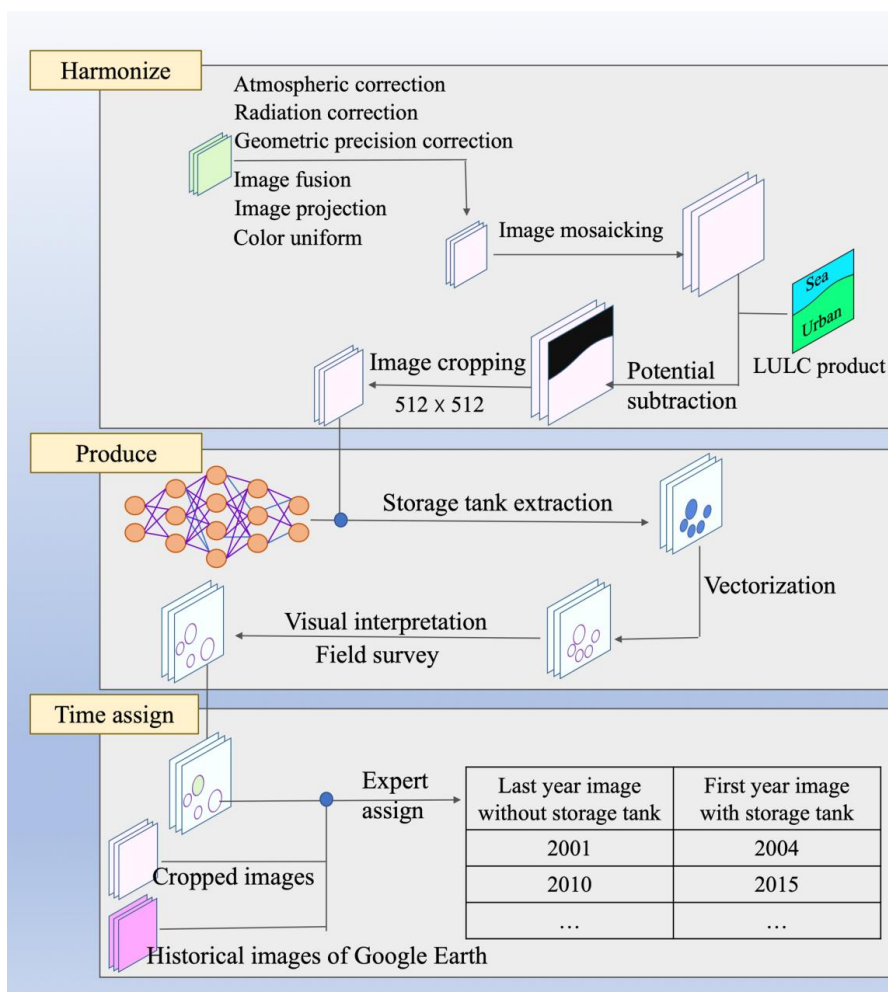


252  
253 *Figure 3. Demonstration of  $\text{CH}_4$  distribution from energetic activities over the study*  
254 *area in the year 2020.*  
255

#### 256 4. Methodology

257 As depicted in Figure 4, the workflow of generating a storage tank dataset consists  
258 of three sections: harmonizing the pixel intensities of different ground objects across  
259 high spatial resolution images captured by different sensors in different study areas;  
260 producing a storage tank dataset by constructing a storage tank extraction model based  
261 on the harmonized high spatial resolution images; assigning the construction year of  
262 each storage tank by multiple experts through visual interpretation referring to the  
263 historical high spatial resolution images, high spatial resolution images collected, and  
264 filed survey from Google Earth.





265

266

Figure 4. Flow chart for storage tank inventory production.

267

#### 268 4.1 Image harmonizing

269 Pixel intensities for ground objects are standardized to ensure consistency across  
 270 the high spatial resolution images collected. This harmonization process mitigates the  
 271 effects of atmospheric variations and discrepancies between imaging sensors captured  
 272 at different times. The standardization includes atmospheric correction, radiometric  
 273 calibration, geometric alignment, image fusion, reprojection, and color normalization.  
 274 In terms of atmospheric correction, the widely used radiation transfer model of the  
 275 second simulation of the satellite signal in the solar spectrum (6S) (Vermote et al., 1997)  
 276 is adopted to determine the atmospheric correction coefficient and eliminate the  
 277 absorption and scattering impact of atmospheric molecules and aerosols for all the  
 278 collected high spatial resolution images. The strategy of local histogram matching



279 (Shen, 2007) is used to correct radiation differences of the same ground object category  
280 in different high spatial resolution images. To improve the geometric precision of the  
281 high spatial resolution images collected, we automatically generated 1000 ground  
282 control points by a widely used key point detector of scale-invariant feature transform  
283 (SIFT) for each city. We calculated the parameters for affine transformation with  
284 reference to the world imagery of Environmental Systems Research Institute (ESRI)  
285 (Hou et al., 2021). Pixel-wise image fusion is conducted on images collected from each  
286 high spatial resolution satellite since they consist of multispectral images with a coarser  
287 spatial resolution than the panchromatic image, as demonstrated in Table 1. To optimize  
288 the utilization of the gathered images, we leveraged the wavelet transform (Sahu and  
289 Sahu, 2014) for the automatic fusion of multispectral and panchromatic images. To  
290 address discrepancies in the projections of the varied high-resolution images we  
291 collected, we standardized all the images to the Universal Transverse Mercator (UTM)  
292 projection using bilinear interpolation for consistency. To maintain visual consistency  
293 across images from different sensors or regions, it is crucial to standardize the color  
294 representation of identical ground objects. In this study, we implemented a nonlinear  
295 stretching technique to modify pixel intensity distribution. This was accomplished by  
296 constructing a color look-up table (Majumder et al., 2000) to ensure uniformity in  
297 spectral intensities across the various images.

298 The harmonized high spatial resolution images were further mosaicked to large  
299 image patches to integrate overlapping areas from adjacent high-resolution images,  
300 ensuring comprehensive coverage and continuity of the observed regions. Referring to  
301 the LULC product of the Esri Land Cover product in 2021, the mosaicked image  
302 patches were subtracted with the ground object category of built area and bare ground,  
303 identified as potential areas with storage tank constructions. Finally, for storage tank  
304 extraction, the subtracted images were cropped to a size of 512×512 pixels, a size  
305 compatible with the computational limits of our GPU hardware.

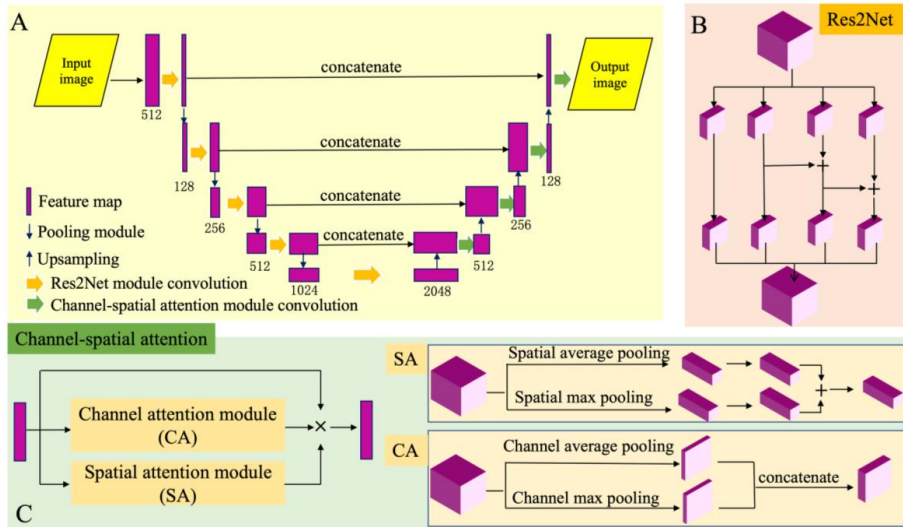
## 306 4.2 Production of storage tank dataset

### 307 4.2.1 Proposed framework for storage tank extraction

308 Stemming from the recently developed semantic segmentation framework for  
309 storage tank extraction, Res2-Unet+ by Yu et al. (Yu et al., 2021), we proposed a new  
310 network structure Res2-UnetA to build storage tank extraction model. As shown in  
311 Figure 5A, our proposed framework integrates the Res2Net module (Figure 5B) and  
312 channel-spatial attention module (Figure 5C) to enhance the significant features for  
313 multi-scale storage tank extraction. During the process of feature map down-scaling,  
314 the Res2Net module can learn the multi-scale features from multiple sub-networks and  
315 concatenate the multi-scale features to enlarge the visual perception capability. In the  
316 stage of feature map up-sampling, our proposed channel-spatial attention module  
317 adopted after each feature map concatenation operation can increase the feature  
318 learning efficiency and enlarge the feature learning scale by synthesizing channel-wise  
319 and spatial attention feature learning modules. Detailed calculation of channel-wise and  
320 spatial attention modules can be referred to Equations (1)-(7). Spatial average pooling  
321 (sa) and spatial maximum pooling (sm) operations are calculated as the average value  
322 and maximum value of input feature map  $f$ , as described in Equations (1)-(2).



323 Correspondingly, the channel-wise average (ca) and maximum pooling (cm) operations  
 324 are the average feature values of all the channels and the maximum feature values of  
 325 all the channels in Equations (3)-(4). The output feature map of the spatial attention  
 326 module (SA) and channel attention module (CA) are calculated according to Equations  
 327 (5)-(6), respectively, and the synthesis of the feature maps from the channel and spatial  
 328 attention modules is organized by multiplication, as illustrated in Equation (7). Through  
 329 multi-scale feature enhancement by our proposed Res2-UnetA framework, it can learn  
 330 the multi-scale storage tank features hierarchically and comprehensively from the high  
 331 spatial resolution images of the different imaging sensors.



332 *Figure 5. Network structure of our proposed Res2-UnetA: (A) network general*  
 333 *demonstration; (B) structure of Res2Net module; (C) structure of channel-spatial*  
 334 *attention module.*  
 335  
 336

$$337 \quad sa_f = \frac{\sum_{i=0}^m \sum_{j=0}^n f_{i,j}}{m \times n} \quad (1)$$

$$338 \quad sm_f = \max (f_{i=0, \dots, m, j=0, \dots, n}) \quad (2)$$

$$339 \quad ca_f = \frac{\sum_{c=0}^h f_{c=k}}{h} \quad (3)$$

$$340 \quad cm_f = \max (f_{c=0, \dots, h}) \quad (4)$$

$$341 \quad SA(f) = conv(conv(sa_f) + conv(sm_f)) \quad (5)$$

$$342 \quad CA(f) = conv(concatenate(ca_f, cm_f)) \quad (6)$$

$$343 \quad CSA(f) = f \times CA(f) \times SA(f) \quad (7)$$

#### 344 4.2.2 Storage tank model construction and dataset generation



345           Based on our proposed framework Res2-UnetA, the pre-processed high spatial  
346 resolution images for the cities of Ningbo, Tangshan, and Dongying are used to train  
347 the storage tank extraction model. Ningbo, Tangshan, and Dongying are three typical  
348 cities in China with large densities of storage tanks so that they can provide large  
349 quantities of training samples with high spectral and textual feature variety in different  
350 sizes. The storage tanks for the training dataset are interpreted visually by three experts  
351 in a relative field referring to the collected high spatial resolution images. The model is  
352 finetuned based on the optimized model from Res2-Unet+ by Yu et al. (Yu et al., 2021)  
353 with a learning rate of 0.01. It converges to the optimum at the iteration of 69.

354           With the optimized model, the storage tanks for the remaining cities are extracted  
355 accordingly and vectorized to the shapefile. While the enhanced model for extracting  
356 storage tanks generally performs well, it's not infallible. Some tanks are inadvertently  
357 missed, and other objects with similar spectral or textural characteristics are  
358 occasionally mistakenly identified as tanks. Therefore, the vectorized shapefile is  
359 further refined manually by visual interpretation with referral to the high spatial  
360 resolution images. Due to the inconsistent spectral intensities for the storage tanks in  
361 the images, triggered by shadows and different viewing angles, the vectorized storage  
362 tanks in the inventory take different shapes. To synchronize the storage tanks in the  
363 inventory taking on a round shape, we re-construct a circle for each extracted storage  
364 tank according to the radius calculated in the inventory, and the inventory is updated  
365 with the re-constructed circle. To facilitate the dating of each storage tank's construction  
366 year, the reconstructed circle for each extracted storage tank has been manually  
367 validated by six experienced experts through visual interpretation based on our  
368 collected high spatial resolution images and field survey.

#### 369 **4.3 Construction year assignment**

370           In the STD dataset we developed, a team of six experts determines the construction  
371 year for each storage tank by conducting visual assessments using high-resolution  
372 historical images available on Google Earth, with the cutoff date for this process being  
373 January 1<sup>st</sup>, 2024. The intermittent availability of historical high-resolution images on  
374 Google Earth poses a challenge in determining the precise construction years for many  
375 storage tanks, especially when images from successive years are missing. We  
376 documented the most recent year when a storage tank was absent (last year image  
377 without storage tank) and the earliest year when it was first observed (first year image  
378 with storage tank) in the historical imagery, as illustrated in Figure 4. The actual  
379 construction year lies within this timeframe. For analysis simplicity, we've designated  
380 each tank's initial observed year as the construction year.

381           Since the high-resolution images used to compile the storage tank dataset were  
382 captured in 2021, it is presumed that all tanks were constructed no later than this year.  
383 However, due to the absence of updated high-resolution imagery on Google Earth, 488  
384 tanks remain undetected in the historical records. For these, the year of construction has  
385 been inferred as 2021, following thorough visual confirmation using the high-resolution  
386 images we have acquired. The considerable lapses in historical high-resolution imagery  
387 on Google Earth necessitate assigning a provisional construction year 2021 to 630  
388 storage tanks. The year of 2021 marks the earliest documented evidence of these tanks'



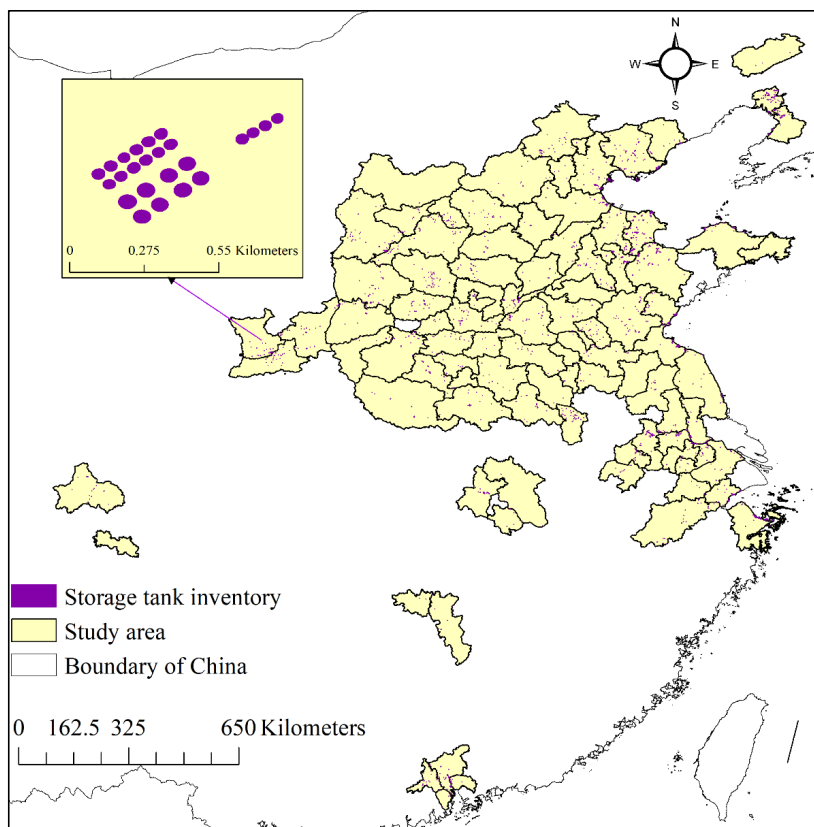
389 existence in the high-resolution images we collected, beyond which no prior images are  
390 available.

391

## 392 **5. Results**

### 393 **5.1 Spatial distribution of storage tanks**

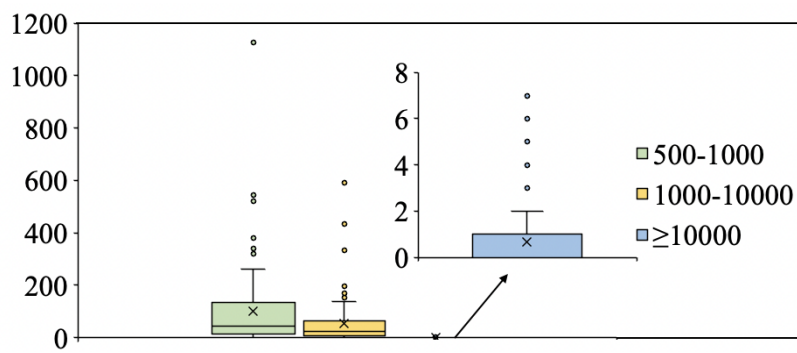
394 Following the workflow in Figure 4, the storage tanks in the 92 typical cities of  
395 China are extracted based on the high spatial resolution images using the trained  
396 semantic segmentation model. Given that large capacity storage tanks are known to  
397 release significant levels of CH<sub>4</sub>, resulting in climate warming, the proposed inventory  
398 focuses on storage tanks with an area of 500 m<sup>2</sup>. 14,461 storage tanks are extracted  
399 from the 92 cities with areas ranging from 500 m<sup>2</sup> to 18,583.15 m<sup>2</sup>. As shown in Figure  
400 6, the storage tanks are distributed unevenly in different cities and reflect different sizes  
401 and spatial distribution patterns. To explore the different distribution patterns, the  
402 storage tanks are categorized into three groups according to the area: 500-1,000 m<sup>2</sup>,  
403 1,000-10,000 m<sup>2</sup>, and ≥10,000 m<sup>2</sup>. The accumulated number of storage tanks of  
404 different sizes for all the cities is compiled as shown in Figure 7. It may be seen that  
405 storage tanks of 500-1000 m<sup>2</sup> are more than those of larger sizes. The relatively smaller  
406 storage tanks are more widely used in industry. Due to the high cost of construction,  
407 considering all the cities, the maximum number of large storage tanks of size ≥10,000  
408 m<sup>2</sup> is found to be seven for the city of Tangshan. Notably, there are few cities with  
409 storage tanks of 10,000 m<sup>2</sup> in size.



410

411

Figure 6. Inventory for storage tanks of the 92 typical cities.



412

413

414

415

416

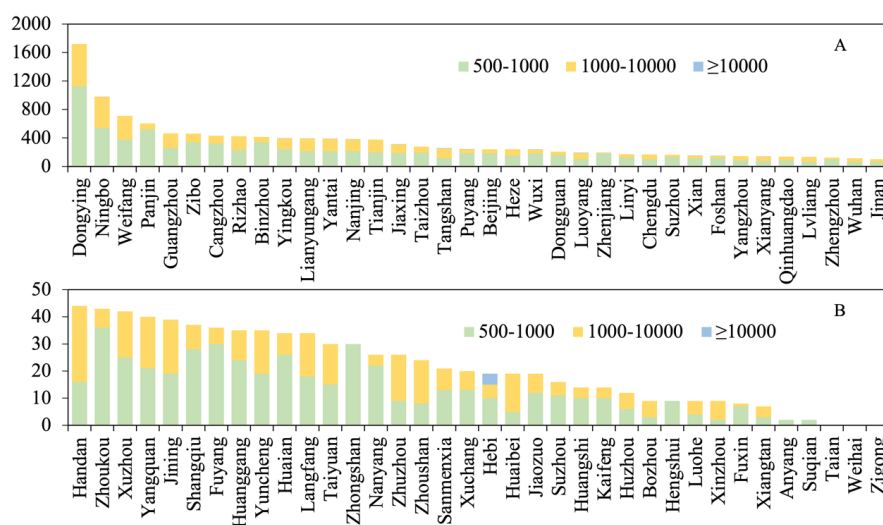
417

Figure 7. Box plot of storage tank distribution for the different size categories ( $m^2$ ) for the 92 cities.

About the 92 cities examined, 38 cities have storage tanks with an accumulated  $\geq 100$ , as shown in Figure 8A. Dongying has the largest accumulated number of 1719,



418 about twice that of Ningbo, the second highest ranked city with 981 storage tanks.  
 419 Weifang and Panjin are next in rank with storage tanks more than 500. The number of  
 420 storage tanks of size 500-1000 m<sup>2</sup> is greater than that for 1,000-10,000 m<sup>2</sup> and ≥10,000  
 421 m<sup>2</sup> for most cities. This finding indicates the widespread use of smaller storage tanks in  
 422 different industries. Furthermore, there are 36 cities with an accumulated number of <  
 423 50 (Figure 8B). Among the 36 cities, Hebi is the only city with four storage tanks of  
 424 ≥10,000 m<sup>2</sup> in size. The other cities, except Tangshan, do not have that large storage  
 425 tanks. No storage tanks of size ≥500 m<sup>2</sup> are observed for the cities of Taian, Weihai,  
 426 and Zigong.



427  
 428 *Figure 8. Number of storage tanks of different size categories in the various cities: (A)*  
 429 *cities with an accumulated storage tank number ≥100; (B) cities with accumulated*  
 430 *storage tank number of <50.*  
 431

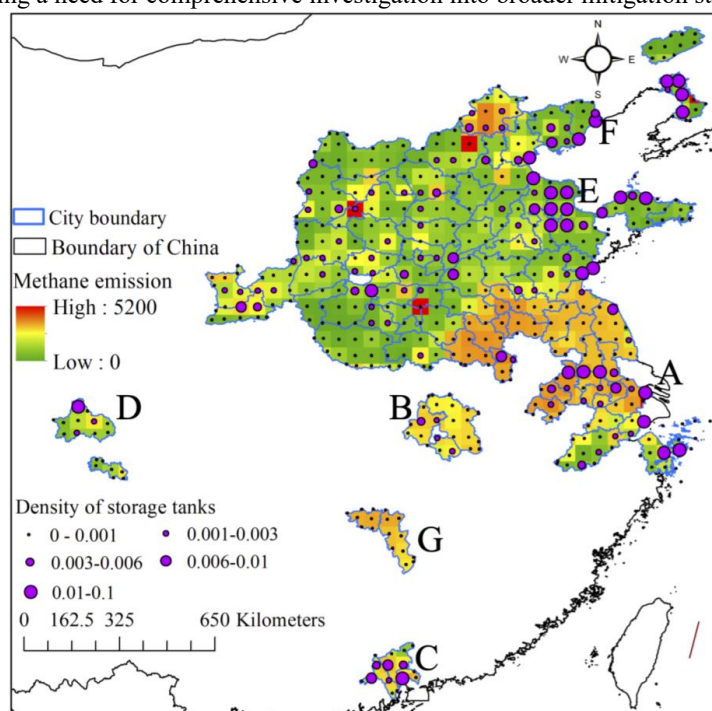
## 432 5.2 Spatial consistency with CH<sub>4</sub> emission

433 To explore whether the distribution patterns of storage tanks influence CH<sub>4</sub>  
 434 emissions significantly, we explored the spatial consistency between estimated CH<sub>4</sub>  
 435 from energy emission products and the density of storage tanks in our proposed dataset  
 436 STD over the study area. Given the coarser spatial resolution of the CH<sub>4</sub> emission  
 437 product at 0.5°, which is less detailed than that of the high spatial resolution images  
 438 used for generating our storage tank dataset, we've calculated storage tank density to  
 439 align with each pixel grid of the CH<sub>4</sub> data. The density is defined by the total storage  
 440 tank area ratio within each corresponding 3025 km<sup>2</sup> pixel grid area (55km × 55km),  
 441 where 55 km is an approximation of 0.5° latitude or longitude at the equator.

442 The storage tank density is calculated for each grid pixel of the CH<sub>4</sub> emission  
 443 product and is demonstrated in Figure 9. We can recognize that large-scale areas with  
 444 high CH<sub>4</sub> emission in the atmosphere generally cluster large densities of storage tanks  
 445 (clustered cases of A, B, C, and D). The sparsely distributed storage tanks with high  
 446 density are mostly accompanied by a higher CH<sub>4</sub> emission than the neighborhood (as



447 shown in cases of E). There are also some cities with a high density of storage tanks  
448 and low CH<sub>4</sub> emission estimation, especially at the border of mainland China, as in the  
449 cases of F. That could be attributed to the coastal air currents, which will likely disperse  
450 CH<sub>4</sub> emissions more effectively. It also needs to be pointed out that for the cities marked  
451 as G in Figure 9, the estimated CH<sub>4</sub> emission is relatively high, but the density of storage  
452 tanks is low. One possible reason is the unrestrained leakage of CH<sub>4</sub> from the storage  
453 tanks, highlighting the urgent need for effective control measures. Alternatively, other  
454 high-energy activities within these regions might be significant CH<sub>4</sub> contributors,  
455 suggesting a need for comprehensive investigation into broader mitigation strategies.



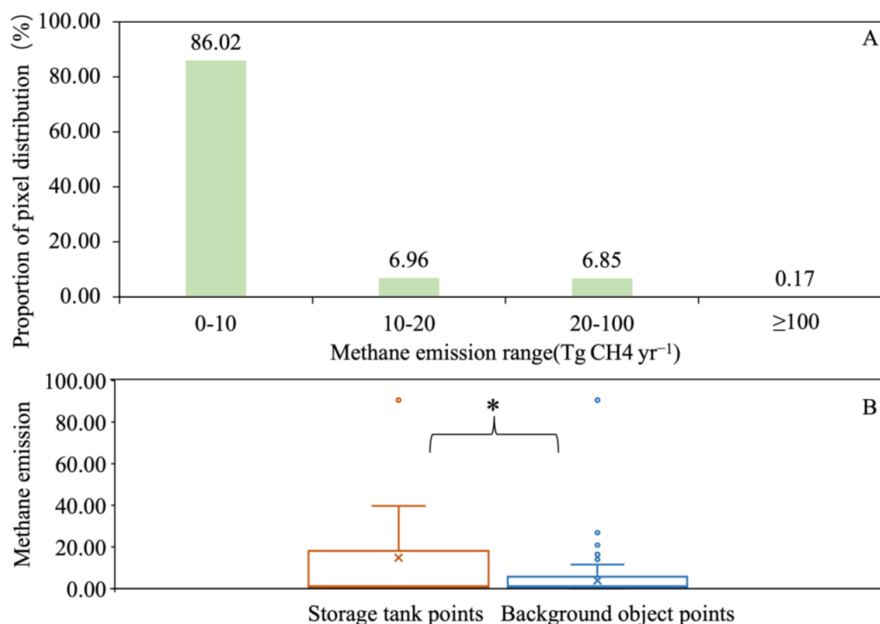
456  
457 *Figure 9. Spatial distribution pattern of different densities of storage tank area with*  
458 *different CH<sub>4</sub> emissions in the atmosphere.*

459 To objectively explore the spatial consistency of storage tank distribution and CH<sub>4</sub>  
460 emission from energetic activities, we randomly selected 4000 storage tank pixels and  
461 4000 background object pixels to evaluate the significance of the impact of storage  
462 tanks on CH<sub>4</sub> emission. Referring to Figure 3, the value of CH<sub>4</sub> emission varies by a  
463 large margin between 0.000055 and 5160.32 Tg CH<sub>4</sub>yr<sup>-1</sup>. The large value gap of CH<sub>4</sub>  
464 emission will cause bias in the differential significance test. We generated the quantity  
465 distribution of pixels with different CH<sub>4</sub> emission value gaps (as shown in Figure 10A)  
466 and found that 99.83% of pixels have a CH<sub>4</sub> emission value of <100 TgCH<sub>4</sub>yr<sup>-1</sup>.  
467 Therefore, the 4000 storage tank pixels and 4000 background object pixels are  
468 randomly selected from pixels with a CH<sub>4</sub> emission value of <100 TgCH<sub>4</sub>yr<sup>-1</sup>. As shown  
469 in Figure 10B, the CH<sub>4</sub> emission values of storage tank pixels are statistically  
470 significantly larger than that of background object pixels with a p-value <0.05. It





471 indicates storage tanks are significant energetic sources of CH<sub>4</sub> emission. With our  
 472 proposed dataset STD, it is possible to monitor the greenhouse gas emissions from  
 473 storage tanks to take effective measurements for potential climate warming reduction  
 474 in time.



475  
 476 *Figure 10. Distribution pattern of storage tank pixels with different CH<sub>4</sub> emission*  
 477 *estimations: (A) Proportion of pixels with different CH<sub>4</sub> emission estimations; (B) box*  
 478 *plot of CH<sub>4</sub> emission of storage tank points and background object points.*  
 479

### 480 5.3 Temporal impact on CH<sub>4</sub> emission

481 Given the constraints of historical high-resolution imagery on Google Earth, the  
 482 earliest ascertainable construction year for storage tanks is set to 2000, with the latest  
 483 capped at 2021, as depicted in Figure 11. Therefore, our dataset STD includes storage  
 484 tanks constructed in years of 2000-2021. It is noted that storage tanks were largely  
 485 constructed in 2009, 2010, 2012, 2013, and 2014, while those in 2000 and 2001 were  
 486 less constructed, with quantities of approximately twenty. To align with the construction  
 487 temporal range of storage tanks in the dataset, CH<sub>4</sub> emission products of 2005, 2010,  
 488 2015, and 2020 are utilized, as these emission products are updated every five years.  
 489 To explore the impact of storage tank construction on CH<sub>4</sub> emission, the storage tanks  
 490 are grouped by the product year of CH<sub>4</sub>, as listed in Table II. Storage tanks built in the  
 491 years 2000 and 2021 are excluded from the impact analysis due to the exceed of the  
 492 corresponding impact temporal range of CH<sub>4</sub> emission.

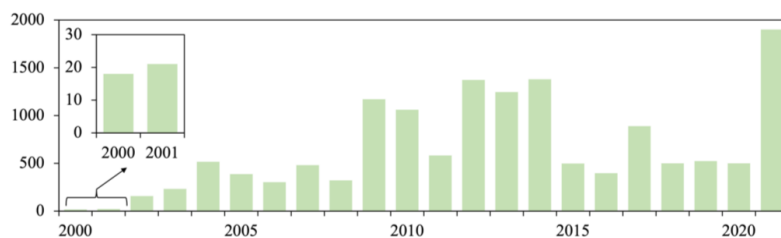
493 Table II. Correspondence between the year of CH<sub>4</sub> emission product and group of  
 494 construction years of storage tanks.

Year of CH <sub>4</sub> emission product	Year group of storage tanks constructed
2005	2001-2005



2010	2006-2010
2015	2011-2015
2020	2016-2020

495



496

Figure 11. Number of storage tanks constructed in different years.

497

498

499

500

501

502

503

504

505

506

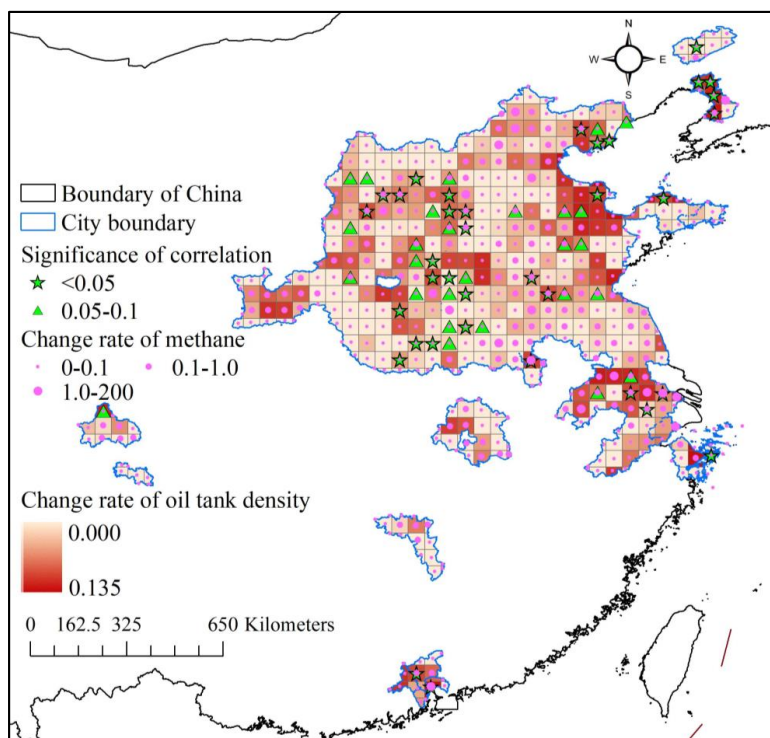
507

508

509

It is noted that the spatial resolution of the CH<sub>4</sub> emission product is coarser than the images we used to generate our proposed STD dataset; similar to the works in spatial consistency exploration, the storage tanks constructed in different groups of years are gridded by the CH<sub>4</sub> emission product, and the density of storage tanks is calculated for each grid. We conducted a correlation analysis to explore the statistical significance of the impact of storage tank construction on CH<sub>4</sub> emission over 2005-2020 at levels of p=0.05 and p=0.1, respectively. Moreover, the rate of CH<sub>4</sub> emission change and oil tank density newly constructed every five years are calculated according to Equation (8) and demonstrated accordingly in Figure 12.

$$R=(I_{2020}-I_{2005})/4 \quad (8)$$



510

511

512

513

Figure 12. Significance of correlation between change rate of oil tank density and  $CH_4$  emission change.

514

515

516

517

518

519

520

521

522

523

524

525

526

527

528

529

530

531

532

Both  $CH_4$  emission and newly constructed storage tank density increased from 2005 to 2020, with positive rates in Figure 12. Over the 92 cities in this study, storage tanks are constantly being constructed to meet the industrial demand, but  $CH_4$  emission is continuously increasing too. The storage tanks of cities such as Yingkou, Panjin, Dongying, Binzhou, Yantai, Weifang, Tangshan, Linyi, Rizhao, Puyang, Xi'an, Pingdingshan, Huainan, Nanjing, Maanshan, Changzhou, Wuxi, Chengdu, Foshan, Dongguan, and Guangzhou are constructed with higher rates than the other cities.  $CH_4$  from energetic activities is emitted at a highly increasing rate in multiple cities, such as Beijing, Yingkou, Zhenjiang, Nanjing, Maanshan, Changzhou, Wuxi, Shijiazhuang, Huainan, and Dongguan. Grids showing a statistically significant correlation ( $p < 0.1$ ) between storage tank density and  $CH_4$  emissions typically display a notable rise in the rate of storage tank density, particularly in grids with a p-value less than 0.05. This trend suggests that areas with active storage tank construction may contribute significantly to increased  $CH_4$  emissions. Some grids exhibit high  $CH_4$  emission increasing rates but low storage tank density increasing rates. This pattern suggests that while storage tank construction significantly contributes to  $CH_4$  emissions, other sources related to energy production, such as the extraction and transport of coal, oil, and natural gas, are also major contributors to  $CH_4$  release. However, regarding the 92 typical cities with intensive storage tank distribution and construction, the impact of storage tank



533 construction on CH<sub>4</sub> emission from energetic activities is largely statistically significant,  
534 especially in areas with a high rate of new storage tank construction. Therefore, it is  
535 necessary to propose effective measurements to mitigate CH<sub>4</sub> emissions from the  
536 continuously constructed storage tanks.

537

## 538 **6. Discussion**

### 539 **6.1 Comparison with published Datasets**

540 To the best of our knowledge, limited research has been published concerning  
541 remote sensing datasets on storage tanks. The dataset, NEPU–OWOD V1.0, is a  
542 recently proposed oil storage tank dataset featuring 1,192 oil storage tanks from 432  
543 images of Google Earth. It covers the city of Daqing on a limited scale. However, the  
544 dataset lacks georeferenced information, hence the difficulty in supporting further  
545 research by governmental agencies and academic groups on various subjects such as  
546 air pollution control and energy consumption balance studies (Wang et al., 2021). This  
547 is similar to the NEPU–OWOD V1.0 dataset, the Oil and Gas Tank Dataset (Rabbi et  
548 al., 2020), which comprises 760 image patches of size 512×512. The images are taken  
549 at a spatial resolution of 30 cm, and the annotations are boundary boxes rather than  
550 details on the exact shape. To assess the national energy demand, an oil storage tank  
551 dataset is released on the platform Kaggle (Heyer, 2019). However, the images are  
552 collected from Google Earth without georeferenced information. Only 100 image  
553 patches of size 512×512 pixels are included in the dataset. Publication of datasets on  
554 oil storage tanks is generally developed to improve automatic methods for the detection  
555 of storage tanks rather than further environmental analysis based on the combination  
556 and synthesis with datasets of other domains, such as air pollution products. Therefore,  
557 the proposed STD dataset is the first storage tank inventory that provides a detailed  
558 distribution of storage tanks of diverse sizes in 92 cities in China. Each storage tank in  
559 the dataset has undergone rigorous verification by six experts. Additionally, the dataset  
560 meticulously logs the construction year for each tank. This allows for an analysis of the  
561 temporal evolution of storage tank distribution and its combined effects with CH<sub>4</sub>  
562 emissions on the climate. Such insights pave the way for developing more effective  
563 energy management and climate change mitigation strategies, serving as a valuable  
564 resource for research in atmospheric science, environmental studies, and sustainable  
565 development.

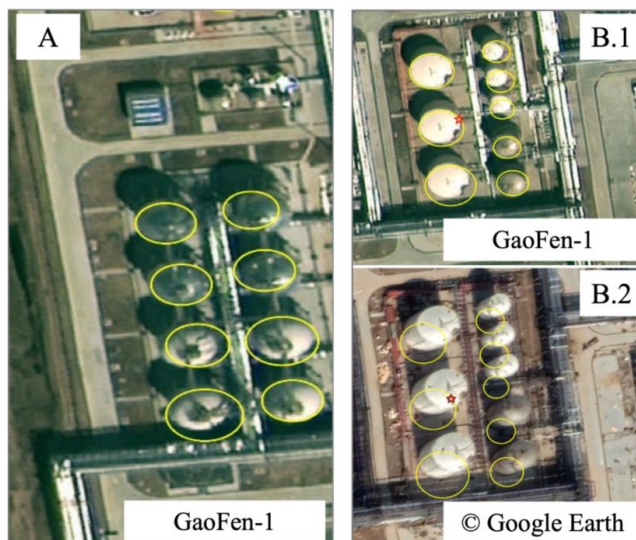
566

### 567 **6.2 Uncertainties, limitations, and implications**

568 The Storage Tank Dataset (STD) we've compiled for 92 cities in China serves as  
569 a valuable tool for climate change research, despite certain limitations. The extraction  
570 process from high-resolution images is subject to inaccuracies due to shadows and the  
571 inherent limitations of representing three-dimensional tanks as two-dimensional circles,  
572 potentially leading to slight positional errors (Figure 13A). Additionally, the variance  
573 in perspective between our collected high spatial resolution images and Google Earth  
574 historical images can cause deviations in visual refinement in the tanks' vectorized  
575 outlines (as shown in Figure 13B). To mitigate these issues, expert analysis is employed



576 to ensure tank identification and location precision, referring to the collected high  
577 spatial resolution images.  
578



579  
580 *Figure 13. Example cases of our proposed STD dataset: (A) cases with shifted circles*  
581 *due to cast by shadow; (B) cases with largely deviated circles in different images*  
582 *due to different viewing angles.*  
583

584 The pioneering STD dataset encompasses georeferenced storage tank shapes for  
585 92 key Chinese cities crafted from high-resolution images. For each storage tank, the  
586 corresponding construction year is assigned, referring to the high-resolution historical  
587 images of Google Earth. It's a versatile resource with spatial and temporal distribution  
588 patterns, not just for mapping CH<sub>4</sub> and other emissions but also for aiding the  
589 development of infrastructural strategies across various industries. However, the dataset  
590 currently lacks volumetric data due to the absence of height measurements for the tanks.  
591 Future enhancements aim to incorporate height data through advanced remote sensing  
592 technologies like SAR imagery, enriching the dataset with three-dimensional accuracy  
593 and providing a more comprehensive understanding of storage tank capacities.  
594

## 595 7. Dataset availability

596 The STD dataset is publicly available as a repository at  
597 <https://zenodo.org/records/10514151> (Chen et al., 2024). The dataset is provided in a  
598 shapefile, wherein a polygon with an area attribute in units of m<sup>2</sup> represents each  
599 storage tank, and two attributes of years, year\_1 indicating the most recent year when  
600 a storage tank was absent (last year image without storage tank) and year\_2 indicating  
601 the earliest year when it was first observed (first year image with storage tank). The  
602 inventory is intended to be used to further analyze the impact on CH<sub>4</sub> emissions, devise  
603 and implement more efficient energy management strategies. Moreover, our approach



604 represents a powerful new source to improve automatic methods for storage tank  
605 extraction from high spatial resolution images, given that it represents a comprehensive  
606 and state-of-the-art inventory with tens of thousands of storage tanks georeferenced of  
607 92 typical cities over China.

## 608 **8. Conclusions**

609 In support of CH<sub>4</sub> emission control to mitigate climate warming, the STD dataset  
610 is proposed by providing a meticulously georeferenced inventory of storage tanks larger  
611 than 500 m<sup>2</sup> across 92 key cities of China in years of 2000-2021. Leveraging a novel  
612 semantic segmentation framework, Res2-UnetA, and rigorous visual interpretation  
613 based on the collected high spatial resolution images, historical high spatial resolution  
614 images from Google Earth, and field survey, the dataset not only details the spatial  
615 distribution of large storage tanks but also includes their construction years. Based on  
616 the STD dataset, the spatial distribution pattern of the storage tanks of different sizes  
617 was analyzed in 92 cities. We also explored the impact of storage tank construction on  
618 CH<sub>4</sub> emission from energetic activities through 2005-2020. Compared with the  
619 published datasets for storage tanks, the STD dataset is the first inventory that compiles  
620 georeferenced storage tanks in 92 cities with detailed shape boundaries and construction  
621 years. In general, publicly available datasets on storage tanks typically cover only part  
622 of a city without georeferenced information and detailed shape boundaries. It is,  
623 therefore, difficult to objectively explore the extent and patterns of environmental  
624 impact and the energy management of the storage tanks at large scale. The STD dataset  
625 enables large-scale environmental impact analysis of storage tanks and their correlation  
626 with CH<sub>4</sub> emissions. It demonstrates strong spatial consistency with CH<sub>4</sub> emissions in  
627 92 typical Chinese cities, highlighting the substantial increase in CH<sub>4</sub> emissions due to  
628 storage tank construction. The storage tank dataset STD can contribute significantly to  
629 supporting energy management strategies and sustainability development studies while  
630 giving direct support to academic research and government agencies.

631

## 632 **Author contributions**

633 FC and LW designed the study and conducted the experiments. YW, HZ, NW, PM and  
634 BY compiled the dataset. BY wrote the manuscript.

635

## 636 **Competing interests**

637 The authors declare that they have no conflicts of interest.

638

## 639 **Financial support**

640 This work was supported by the National Key R&D Program of China (No.  
641 2022YFC3800701), the Youth Innovation Promotion Association, CAS (2022122), the



642 China-ASEAN Big Earth Data Platform and Applications (CADA, guikeAA20302022).

643

## 644 References

- 645 Amann, M., Bertok, I., Borken-Kleefeld, J., Cofala, J., Heyes, C., Höglund-Isaksson, L., Klimont,  
646 Z., Nguyen, B., Posch, M., and Rafaj, P.: Cost-effective control of air quality and greenhouse gases  
647 in Europe: Modeling and policy applications, *Environmental Modelling & Software*, 26, 1489-1501,  
648 2011.
- 649 Badrinarayanan, V., Kendall, A., and Cipolla, R.: Segnet: A deep convolutional encoder-decoder  
650 architecture for image segmentation, *IEEE transactions on pattern analysis and machine intelligence*,  
651 39, 2481-2495, 2017.
- 652 Chen, F., Wang, N., Yu, B., and Wang, L.: Res2-Unet, a new deep architecture for building detection  
653 from high spatial resolution images, *IEEE Journal of Selected Topics in Applied Earth Observations  
654 and Remote Sensing*, 15, 1494-1501, 2022.
- 655 Chen, F., Wang, J., Li, B., Yang, A., and Zhang, M.: Spatial variability in melting on Himalayan  
656 debris-covered glaciers from 2000 to 2013, *Remote Sensing of Environment*, 291, 113560,  
657 <https://doi.org/10.1016/j.rse.2023.113560>, 2023.
- 658 Chen, F., Wang, L., Wang, Y., Zhang, H., Wang, N., Ma, P., and Yu, B. (2024). Retrieval of dominant  
659 methane (CH<sub>4</sub>) emission sources, the first high resolution(1-2m) dataset of storage tank in China in 2021,  
660 Zenodo [data set], <https://zenodo.org/records/10514151>, 2024
- 661 Chen, L.-C., Papandreou, G., Schroff, F., and Adam, H.: Rethinking atrous convolution for semantic  
662 image segmentation, arXiv preprint arXiv:1706.05587, 2017a.
- 663 Chen, L.-C., Papandreou, G., Kokkinos, I., Murphy, K., and Yuille, A. L.: Deeplab: Semantic image  
664 segmentation with deep convolutional nets, atrous convolution, and fully connected crfs, *IEEE  
665 transactions on pattern analysis and machine intelligence*, 40, 834-848, 2017b.
- 666 Crippa, M., Oreggioni, G., Guizzardi, D., Muntean, M., Schaaf, E., Lo Vullo, E., Solazzo, E.,  
667 Monforti-Ferrario, F., Olivier, J. G., and Vignati, E.: Fossil CO<sub>2</sub> and GHG emissions of all world  
668 countries, Publication Office of the European Union: Luxemburg, 2019.
- 669 Ding, T., Ning, Y., and Zhang, Y.: Estimation of greenhouse gas emissions in China 1990–2013,  
670 *Greenhouse Gases: Science and Technology*, 7, 1097-1115, 2017.
- 671 Fan, L., Chen, X., Wan, Y., and Dai, Y.: Comparative Analysis of Remote Sensing Storage Tank  
672 Detection Methods Based on Deep Learning, *Remote Sensing*, 15, 2460, 2023.
- 673 Gao, S.-H., Cheng, M.-M., Zhao, K., Zhang, X.-Y., Yang, M.-H., and Torr, P.: Res2net: A new multi-  
674 scale backbone architecture, *IEEE transactions on pattern analysis and machine intelligence*, 43,  
675 652-662, 2019.
- 676 Heyer, K.: Airbus oil storage detection, 2019.
- 677 Hoesly, R. M., Smith, S. J., Feng, L., Klimont, Z., Janssens-Maenhout, G., Pitkanen, T., Seibert, J.  
678 J., Vu, L., Andres, R. J., and Bolt, R. M.: Historical (1750–2014) anthropogenic emissions of



- 679 reactive gases and aerosols from the Community Emissions Data System (CEDS), Geoscientific  
680 Model Development, 11, 369-408, 2018.
- 681 Hou, B., Ren, Z., Zhao, W., Wu, Q., and Jiao, L.: Object detection in high-resolution panchromatic  
682 images using deep models and spatial template matching, IEEE Transactions on Geoscience and  
683 Remote Sensing, 58, 956-970, 2019.
- 684 Hou, D., Miao, Z., Xing, H., and Wu, H.: Two novel benchmark datasets from ArcGIS and bing  
685 world imagery for remote sensing image retrieval, International Journal of Remote Sensing, 42,  
686 240-258, 2021.
- 687 Im, S., Mostafa, A., Lim, K.-H., Kim, I., and Kim, D.-H.: Automatic temperature rise in the manure  
688 storage tank increases methane emissions: Worth to cool down!, Science of The Total Environment,  
689 823, 153533, 2022.
- 690 Johnson, D., Clark, N., Heltzel, R., Darzi, M., Footer, T. L., Herndon, S., and Thoma, E. D.: Methane  
691 emissions from oil and gas production sites and their storage tanks in West Virginia, Atmospheric  
692 Environment: X, 16, 100193, 2022.
- 693 Karra, K., Kontgis, C., Statman-Weil, Z., Mazzariello, J. C., Mathis, M., and Brumby, S. P.: Global  
694 land use/land cover with Sentinel 2 and deep learning, 2021 IEEE international geoscience and  
695 remote sensing symposium IGARSS, 4704-4707,
- 696 Kirschke, S., Bousquet, P., Ciais, P., Saunois, M., Canadell, J. G., Dlugokencky, E. J., Bergamaschi,  
697 P., Bergmann, D., Blake, D. R., Bruhwiler, L., Cameron-Smith, P., Castaldi, S., Chevallier, F., Feng,  
698 L., Fraser, A., Heimann, M., Hodson, E. L., Houweling, S., Josse, B., Fraser, P. J., Krummel, P. B.,  
699 Lamarque, J.-F., Langenfelds, R. L., Le Quéré, C., Naik, V., O'Doherty, S., Palmer, P. I., Pison, I.,  
700 Plummer, D., Poulter, B., Prinn, R. G., Rigby, M., Ringeval, B., Santini, M., Schmidt, M., Shindell,  
701 D. T., Simpson, I. J., Spahni, R., Steele, L. P., Strode, S. A., Sudo, K., Szopa, S., van der Werf, G.  
702 R., Voulgarakis, A., van Weele, M., Weiss, R. F., Williams, J. E., and Zeng, G.: Three decades of  
703 global methane sources and sinks, Nature Geoscience, 6, 813-823, 10.1038/ngeo1955, 2013.
- 704 Kurokawa, J., Ohara, T., Morikawa, T., Hanayama, S., Janssens-Maenhout, G., Fukui, T.,  
705 Kawashima, K., and Akimoto, H.: Emissions of air pollutants and greenhouse gases over Asian  
706 regions during 2000–2008: Regional Emission inventory in ASia (REAS) version 2, Atmospheric  
707 Chemistry and Physics, 13, 11019-11058, 2013.
- 708 Lane, K.: IEA Energy Efficiency 2018 and World Energy Outlook 2018, Brussels, November, 27,  
709 2018.
- 710 Lin, X., Zhang, W., Crippa, M., Peng, S., Han, P., Zeng, N., Yu, L., and Wang, G.: A comparative  
711 study of anthropogenic CH<sub>4</sub> emissions over China based on the ensembles of bottom-up inventories,  
712 Earth Syst. Sci. Data, 13, 1073-1088, 10.5194/essd-13-1073-2021, 2021.
- 713 Long, J., Shelhamer, E., and Darrell, T.: Fully convolutional networks for semantic segmentation,  
714 Proceedings of the IEEE conference on computer vision and pattern recognition, 3431-3440,
- 715 Majumder, A., He, Z., Towles, H., and Welch, G.: Achieving color uniformity across multi-projector  
716 displays, Proceedings Visualization 2000. VIS 2000 (Cat. No. 00CH37145), 117-124,





- 717 Montzka, S. A., Dlugokencky, E. J., and Butler, J. H.: Non-CO<sub>2</sub> greenhouse gases and climate  
718 change, *Nature*, 476, 43-50, 2011.
- 719 O'DUDA, R.: Use of Hough transformation to detect lines and curves in picture, *CACM*, 15, 11-15,  
720 1972.
- 721 Peng, S., Piao, S., Bousquet, P., Ciais, P., Li, B., Lin, X., Tao, S., Wang, Z., Zhang, Y., and Zhou, F.:  
722 Inventory of anthropogenic methane emissions in mainland China from 1980 to 2010, *Atmospheric*  
723 *Chemistry and Physics*, 16, 14545-14562, 2016.
- 724 Rabbi, J., Ray, N., Schubert, M., Chowdhury, S., and Chao, D.: Small-Object Detection in Remote  
725 Sensing Images with End-to-End Edge-Enhanced GAN and Object Detector Network,  
726 10.3390/rs12091432, 2020.
- 727 Ronneberger, O., Fischer, P., and Brox, T.: U-net: Convolutional networks for biomedical image  
728 segmentation, *Medical Image Computing and Computer-Assisted Intervention–MICCAI 2015:*  
729 *18th International Conference, Munich, Germany, October 5-9, 2015, Proceedings, Part III* 18, 234-  
730 241,
- 731 Sahu, V. and Sahu, D.: Image fusion using wavelet transform: a review, *Global Journal of Computer*  
732 *Science and Technology*, Global Journals Inc.(USA), ISSN, 975, 4172, 2014.
- 733 Shen, D.: Image registration by local histogram matching, *Pattern Recognition*, 40, 1161-1172, 2007.
- 734 Stocker, T.: *Climate change 2013: the physical science basis: Working Group I contribution to the*  
735 *Fifth assessment report of the Intergovernmental Panel on Climate Change*, Cambridge university  
736 press2014.
- 737 Venter, Z. S., Barton, D. N., Chakraborty, T., Simensen, T., and Singh, G.: Global 10 m Land Use  
738 Land Cover Datasets: A Comparison of Dynamic World, World Cover and Esri Land Cover, *Remote*  
739 *Sensing*, 14, 4101, 2022.
- 740 Vermote, E. F., Tanré, D., Deuze, J. L., Herman, M., and Morcette, J.-J.: Second simulation of the  
741 satellite signal in the solar spectrum, 6S: An overview, *IEEE transactions on geoscience and remote*  
742 *sensing*, 35, 675-686, 1997.
- 743 Wang, H., Sun, S., Nie, L., Zhang, Z., Li, W., and Hao, Z.: A review of whole-process control of  
744 industrial volatile organic compounds in China, *Journal of Environmental Sciences*, 2022.
- 745 Wang, Z., Bai, L., Song, G., Zhang, J., Tao, J., Mulvenna, M. D., Bond, R. R., and Chen, L.: An Oil  
746 Well Dataset Derived from Satellite-Based Remote Sensing, 10.3390/rs13061132, 2021.
- 747 Wu, Q., Zhang, B., Xu, C., Zhang, H., and Wang, C.: Dense Oil Tank Detection and Classification  
748 via YOLOX-TR Network in Large-Scale SAR Images, *Remote Sensing*, 14, 3246, 2022.
- 749 Xia, X., Liang, H., RongFeng, Y., and Kun, Y.: Oil tank extraction in high-resolution remote sensing  
750 images based on deep learning, *2018 26th International Conference on Geoinformatics*, 1-6,
- 751 Yang, L., Meng, X., and Zhang, X.: SRTM DEM and its application advances, *International Journal*  
752 *of Remote Sensing*, 32, 3875-3896, 2011.
- 753 Yu, B., Chen, F., Wang, N., Wang, L., and Guo, H.: Assessing changes in nighttime lighting in the



- 754 aftermath of the Turkey-Syria earthquake using SDGSAT-1 satellite data, *The Innovation*, 4, 100419,  
755 2023a.
- 756 Yu, B., Xu, C., Chen, F., Wang, N., and Wang, L.: HADeenNet: A hierarchical-attention multi-scale  
757 deconvolution network for landslide detection, *International Journal of Applied Earth Observation*  
758 and *Geoinformation*, 111, 102853, 2022a.
- 759 Yu, B., Yang, A., Chen, F., Wang, N., and Wang, L.: SNNFD, spiking neural segmentation network  
760 in frequency domain using high spatial resolution images for building extraction, *International*  
761 *Journal of Applied Earth Observation and Geoinformation*, 112, 102930, 2022b.
- 762 Yu, B., Chen, F., Ye, C., Li, Z., Dong, Y., Wang, N., and Wang, L.: Temporal expansion of the  
763 nighttime light images of SDGSAT-1 satellite in illuminating ground object extraction by joint  
764 observation of NPP-VIIRS and sentinel-2A images, *Remote Sensing of Environment*, 295, 113691,  
765 <https://doi.org/10.1016/j.rse.2023.113691>, 2023b.
- 766 Yu, B., Chen, F., Wang, Y., Wang, N., Yang, X., Ma, P., Zhou, C., and Zhang, Y.: Res2-Unet+, a  
767 Practical Oil Tank Detection Network for Large-Scale High Spatial Resolution Images, *Remote*  
768 *Sensing*, 13, 4740, 2021.
- 769 Yuen, H., Princen, J., Illingworth, J., and Kittler, J.: Comparative study of Hough transform methods  
770 for circle finding, *Image and vision computing*, 8, 71-77, 1990.
- 771 Zalpour, M., Akbarizadeh, G., and Alaei-Sheini, N.: A new approach for oil tank detection using  
772 deep learning features with control false alarm rate in high-resolution satellite imagery, *International*  
773 *Journal of Remote Sensing*, 41, 2239-2262, 10.1080/01431161.2019.1685720, 2020.
- 774 Zhang, L. and Liu, C.: Oil tank extraction based on joint-spatial saliency analysis for multiple SAR  
775 images, *IEEE Geoscience and Remote Sensing Letters*, 17, 998-1002, 2019.
- 776 Zhang, Z., Hu, S., and Jing, Y.: 2060 China Carbon Neutral-Fossil Energy to Fossil Resource Age,  
777 *Mod. Chem*, 41, 1-5, 2021.
- 778 Zhao, H., Shi, J., Qi, X., Wang, X., and Jia, J.: Pyramid scene parsing network, *Proceedings of the*  
779 *IEEE conference on computer vision and pattern recognition*, 2881-2890